Journal of Hydraulic Research Vol. 56, No. 2 (2018), pp. 282–290
https://doi.org/10.1080/00221686.2017.1313320

Technical note

Image thresholding process for combining photometry with intrusive flow instruments

RICHARD I. WILSON (IAHR Member), PhD Candidate, *Department of Civil & Environmental Engineering, University of Auckland, Auckland, New Zealand*
Email: rwil281@aucklanduni.ac.nz (author for correspondence)

HEIDE FRIEDRICH (IAHR Member), Senior Lecturer, *Department of Civil & Environmental Engineering, University of Auckland, Auckland, New Zealand*
Email: h.friedrich@auckland.ac.nz

CRAIG STEVENS, Principal Scientist Marine Physics, Associate Professor, *National Institute of Water and Atmospheric Research, Wellington, New Zealand*; *Department of Physics, University of Auckland, Auckland, New Zealand*
Email: craig.stevens@niwa.co.nz

ABSTRACT
A novel photometric thresholding process for the study of opaque, sediment-laden flows is presented. The method has been developed to allow photometry and visually intrusive, conventional flow measurement instruments to be used simultaneously. Sediment-laden gravity currents of varying densities were released in a lock-exchange flume containing intrusive ultrasonic Doppler velocity profiling (UVP) probes, siphon tubes and a basal obstacle. A new approach to flume illumination and development of a binary noise-reducing algorithm suited to turbidity currents are presented. Additionally, a standard deviation filtering procedure is introduced. The combined process improves the visibility of opaque currents and optimizes current front recognition around visual obstructions. This offers a key advancement to previous photometric techniques and provides a practical way forward for laboratory experiments on sediment-laden flows.

Keywords: Buoyancy; obstacle; sediment-laden flow; turbidity; visualization

1 Introduction

Sediment-laden underflows are a dynamic fluid process, which occur in riverine, limnic, marine and atmospheric environments. Often referred to as turbidity currents, they are caused by the difference in density between an ambient fluid and an introduced fluid, laden with suspended sediment. This ultimately causes a propagating flow. In a marine setting, turbidity currents pose a significant risk to submarine cables where they are known to have caused breakage following earthquakes and flood events (Carter, Milliman, Talling, Gavey, & Wynn, 2012; Cattaneo et al., 2012; Heezen & Ewing, 1952; Hsu et al., 2008).

Photometry, using visual data from laboratory experiments, has been a key approach to advance our understanding of turbidity currents' flow characteristics, all the more with ongoing headway in digital imagery. It has found particular use for tracking frontal velocities of turbidity currents. Typically, the approach tracks the outline of the current using some form of optical thresholding (Dai, 2014; Jacobson & Testik, 2014; Lombardi, Adduce, Sciortino, & La Rocca, 2015; Mirajkar, Tirodkar, & Balasubramanian, 2015; Nogueira, Adduce, Alves, & Franca, 2013a). A key point of photometry is its non-intrusiveness on flow, in contrast to conventional flow measurement techniques such as acoustic Doppler velocimetry (ADV), density sampling and ultrasonic Doppler velocity profiling (UVP). However, it is not a complete replacement of conventional, intrusive techniques. For example, due to the opaque nature of sediment-laden flows, photometry is unsuitable for quantifying density or velocity profiles within the current body, which are key properties for understanding flow characteristics and development (Jacobson & Testik, 2013; Sequeiros, Naruse, Endo, Garcia, & Parker, 2009; Stagnaro & Bolla Pittaluga, 2014). Previous studies have adopted a combination of photometric and intrusive measurement techniques, however generally not simultaneously used for

Received 10 May 2016; accepted 25 March 2017/Open for discussion until 31 October 2018.

ISSN 0022-1686 print/ISSN 1814-2079 online
http://www.tandfonline.com

experiments (Ghilardi, Franca, & Schleiss, 2014; Jacobson & Testik, 2013).

A simultaneous measurement approach is desirable as it allows for two key benefits: (i) improved efficiency of testing programmes, and (ii) removal of the uncertainty associated with combining different finescale sampling methods from repeated experiments. The primary difficulty with combining techniques, however, is that conventional measurement instruments unavoidably obstruct the view of the flow. Previous studies that have combined techniques provide limited insights into their methodology, and do not elucidate provisions made for the visual obstructions (Sequeiros et al., 2009).

The present study presents the development of a photometric binary thresholding process for opaque turbidity currents, which improves images of flows with visual obstructions. Turbidity currents of ranging densities were released in a lock-box flume containing UVP probes and siphoning racks. Their passage through an obstructed analysis area was captured with a complementary metal-oxide-semiconductor (CMOS) camera. A rectangular obstacle, representing a basic submerged structure, was also installed within the analysis area. This was used to assess the technique's feasibility for future testing with other obstacles, such as cylinders representing submarine cables and piles. A novel method is developed optimizing flume illumination, and binary image thresholding is developed to improve accuracy of current front recognition as it passes the obstructions. A sequence of time series filtering techniques is introduced and their usefulness demonstrated.

2 Experimental set-up and methodology

The enhanced experimental approach was demonstrated using experiments carried out in a lock-exchange flume in the Hydraulic Engineering Laboratory at the University of Auckland. The 5 m long and 400 mm wide acrylic flume had a 580 mm long lock-box and release gate situated at the upstream end. Similarly, a 580 mm long, 660 mm deep sump was located at the downstream end to retard reflection of the sediment-laden current from the back wall (Fig. 1). For all experiments, the flume was filled with tap water to a height, h_0, at the gate. Prior to release of the gate, the temperature of the ambient water was recorded to calculate the interstitial density, ρ_W. An acrylic, rectangular obstacle of width 140 mm and height 50 mm was installed on the flume bed at a location of 3700 mm from the lock-box gate. This location was chosen to minimize surface disturbances created from release of the lock-box gate.

A Lumenera LT425 CMOS 4.0 megapixel camera (Lumenera Corporation, Canada) was installed adjacent to the obstacle to record photometric data of the turbidity current interacting with the obstacle. The camera was coupled with a NIKKOR 50 mm f/1.8 fixed lens (Nikon Corporation, Japan) and centred on the obstacle, creating an analysis area of height 350 mm and width 590 mm. The analysis area was outlined with a vertical and horizontal ruler attached to the viewing wall of the flume. The camera was located at a distance from the flume (approx. 2100 mm), where the 2048 pixel width of the image sensor was optically aligned to the 590 mm extent of the horizontal ruler. Vertical alignment was obtained by pairing the lower boundary of the image sensor with the base of the horizontal ruler. Prior to recording, the vertical resolution of the camera was adjusted to 1504 pixels and set with a recording framerate, $F = 120\ \mathrm{s}^{-1}$.

An array of UVP transducers and density siphons were present within the analysis area. Data obtained from these instruments were not used in this study. However, future studies are planned to combine photometric and ultrasonic measurement techniques. Therefore, their influence on the quality of photometric data is important.

2.1 *Lighting calibration*

In addition to maintaining a low spatial area to pixel ratio and capture frequency, adequate illumination of the analysis area is required to produce high quality images. A key limitation of existing thresholding techniques is that they have typically been optimized for transparent, saline flows (Dai, 2013; Longo,

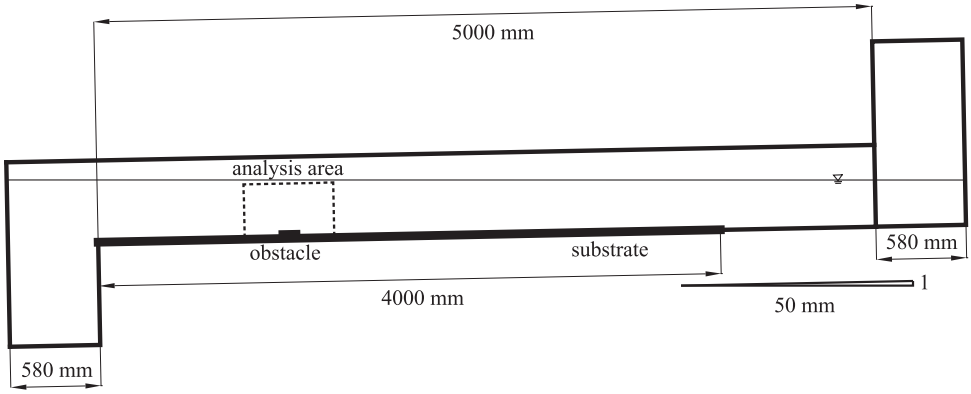

Figure 1 Schematic diagram of the acrylic lock-box flume used for experiments. A manual gate was located at the upstream end of the flume to release the turbidity current, whilst a sump was located at the downstream end to minimize current reflection. A rectangular obstacle was located on the flume bed at a distance of 3700 mm from the gate

Ungarish, Di Federico, Chiapponi, & Maranzoni, 2015; Marino, Thomas, & Linden, 2005; Marleau, Flynn, & Sutherland, 2015). These studies have relied on background or plan lighting to create a high-contrast silhouette of the current boundary for accurate boundary delineation. Whilst this lighting method can be applied to opaque, sediment-laden flows, it becomes impractical if simultaneously combined with conventional, visually intrusive measurement instruments or basal obstacles. This is because the boundary of the current becomes visually obstructed behind the instruments and cannot be continuously traced. The opaque turbidity current also blocks visible flow structures and qualitative characteristics within the head and body of the current.

To optimize the lighting configuration, three plan-elevation combinations of point-source halogen lamps and LED strip lighting were tested. Illuminance was measured at four different locations to compare variance (see Fig. 2). A series of test currents were trialled and the accuracy of boundary recognition for each lighting configuration was compared. Care was taken to paint the flume bed, back wall, and instrument racks black to create a higher contrast with the passing current. The optimum lighting configuration was found to include four 500 W halogen lamps parallel to the flume and four 500 W halogen lamps in plan above the analysis area, powered at 240 V. The plan halogen lamps were dimmed to 90 V using two Variac voltage transformers to reduce over-exposure of the captured images. Further details of the trial study were documented by Wilson (2015).

2.2 *Test procedure*

A total of 16 tests were completed within the flume. The tested turbidity currents had initial theoretical densities ρ, of 1020, 1040, 1060 and 1080 kg m^{-3}. They were comprised of a 1:1 ratio by mass of Ballotini spherical glass beads and kaolinite clay. The four initial densities were tested for four different obstacle and substrate configurations; smooth bed-obstacle, rough bed obstacle, rough bed-no obstacle, and smooth bed-no obstacle. The rough bed comprised of 0.85 mm sand (D_{50}) glued to a steel sheet of length 4000 mm (Fig. 1). The theoretical volume of sediment slurry for each test was displaced from the lock-box prior to addition of the slurry, to minimize the creation of free surface waves.

The prepared sediment mixture was mechanically mixed for a minimum of 30 s in a bucket. Temperature readings of the ambient water in the flume were taken to ensure the correct theoretical density of the ambient fluid. The LT425 camera was then manually focused on the vertical ruler. The sediment slurry was mixed for a further 10 s and added to the lock-box. The gate was then fully opened, initiating a propagating turbidity current. When the current had reached a distance of approximately 2.5 m, the LT425 camera commenced recording, and subsequently ceased a minimum of 30 s after the current had traversed the obstacle, or the centre of the analysis area.

3 Spatiotemporal mapping and velocity tracking of current front

The spatiotemporal mapping of the turbidity current boundary is achieved through a sequence of steps. Raw images obtained from the LT425 were captured using Streampix 6 software (NorPix, Inc., Canada), where a green-blue-red-green (GBRG) pattern Bayer filter was applied to all images, which were subsequently exported to JPEG format. JPEG was chosen over TIFF

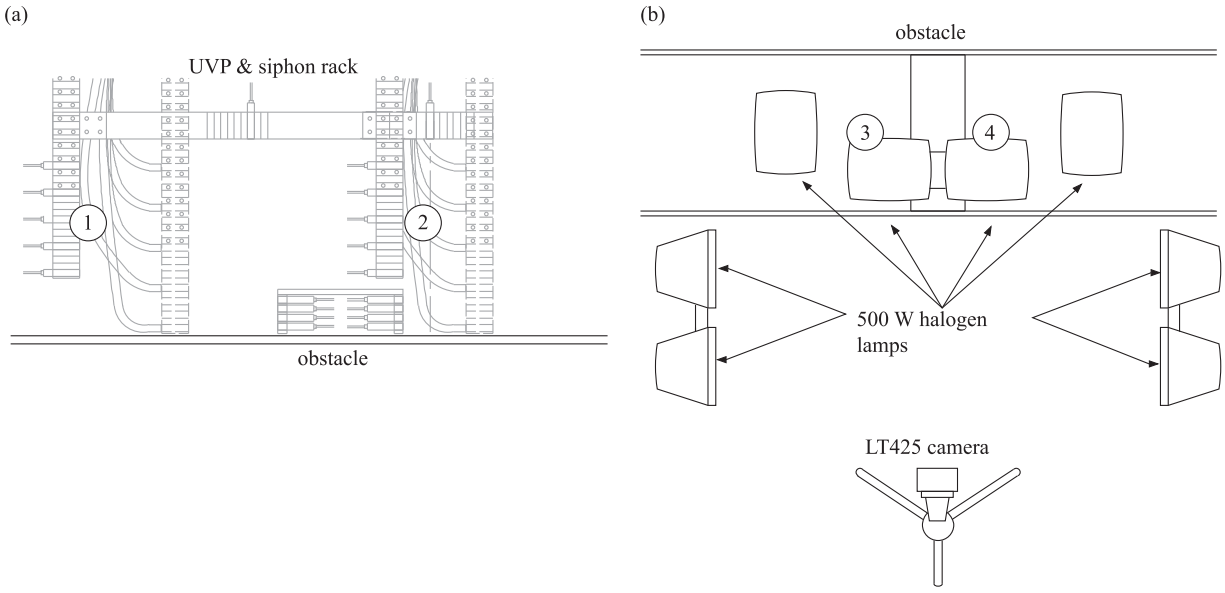

Figure 2 (a) Configuration of rectangular obstacle, surrounding UVP and density siphon racks within the analysis area; (b) plan view of the lighting and camera configuration surrounding the analysis area. Four 500 W halogen lamps were installed parallel to the flume wall, whilst an additional four were installed directly above the analysis area. Numbers 1–4 indicate where illuminance was measured, as documented by Wilson (2015)

and BMP formats due to the significantly lower file size and processing time. A quality comparison with TIFF files showed the mean difference in both calculated velocity and nose location was 2.07% and 0.06%, respectively; thus, JPEG was considered more suitable. All images were batch-processed in Adobe Photoshop CS6 (Adobe Systems, Inc., USA) to correct for barrel lens distortion. Next, images were imported to MATLAB R2013b (The MathWorks, Inc., USA) to apply a series of image manipulation and filtering techniques, as explained below.

Background subtraction was first applied to all images to remove unwanted background noise including unwanted reflections from instrument racks. For each test, 100 frames recorded prior to entry of the current were averaged to account for the sinusoidal flickering of the AC-powered lamps. This average control image was then subtracted from each lens corrected frame. All images were then rotated to account for the 2% slope of the flume bed.

For each test, an arbitrary distortion-corrected image was used to convert pixel values to metric values. It is commonly assumed for confined gravity currents that flow can be represented as two-dimensional, where the current is continuous in nature across the width of the flume (Jacobson & Testik, 2014; Nogueira, Adduce, Alves, & Franca, 2014). Hence spatial calibration is usually conducted at the front or rear wall of the flume (Jacobson & Testik, 2014; Sequeiros et al., 2009). However, what is often overlooked or seldom detailed, is that the perceived location of the current front changes as it propagates through the image area, regardless of lighting orientation. This means that true spatial calibration should be dynamic. Therefore, for this study spatial calibration was achieved by measuring the pixel distance of the known metric distances along the centreline of the water-filled flume, with a range of error provided to account for varying changes in perspective. The laser-cut UVP racks, located in the centreline, were spaced at a distance of 361.45 mm. For each test, the mean of three horizontal measurements at varying heights of the racks was taken as the central pixel calibration factor, Γ (Table 1). These factors ranged from 0.307 to 0.310 mm/pixel, a notably higher resolution than previous studies (Chowdhury & Testik, 2014; Lombardi et al., 2015; Mirajkar et al., 2015). Pixel measurements were also taken at the front and rear width of the obstacle to provide a range of error. The front and rear calibration factors showed a mean difference to the central factor of -4.4% and $+6.0\%$, respectively, which was considered acceptable. These error limits are directly applicable to velocity measurements given in Section 4.

Accounting for change in perspective is also important for lineal measurements of the current nose, x. The camera was positioned so that the upstream face of the obstacle ($x/x_0 \approx 0.38$) had a constant pixel distance from either side of the image. Therefore, at this location and assuming a two dimensional flow, the current nose has no perceived variance in location across the width of the flume. Using the three calibration factors, metric distances in either horizontal direction from this location were found to have a diverging error of less than -4.1% and $+6.3\%$. This difference was considered acceptable; hence the central calibration factor was adopted for all measurements.

Images were then cropped to the final analysis area, which measured approximately 580 mm × 355 mm. The final pixel resolution of each test is shown in Table 1. Horizontal and vertical pixel dimensions had a variance of 0.5% and 0.4% from their means, respectively.

After images had been cropped, they were converted to greyscale and subsequently binary images by applying a light intensity threshold level, I, to each test (Table 1). The threshold

Table 1 Test parameters

Exp. no.	Substrate/obstacle condition	T (°C)	P (kg m^{-3})	ρ_w (kg m^{-3})	Cropped image resolution (pixels)	N	I	Γ (mm/pixel)
NS1	Smooth bed – no obstacle	22.5	1020	997.66	1973 × 1209	750	0.10	0.309
NS2	Smooth bed – no obstacle	18.5	1040	998.50	1978 × 1209	446	0.10	0.309
NS3	Smooth bed – no obstacle	18.5	1060	998.50	1978 × 1209	405	0.10	0.310
NS4	Smooth bed – no obstacle	18.5	1080	998.50	1978 × 1209	308	0.10	0.309
NR1	Rough bed – no obstacle	22.0	1020	997.77	1973 × 1209	788	0.10	0.309
NR2	Rough bed – no obstacle	23.0	1040	997.54	1975 × 1214	465	0.10	0.309
NR3	Rough bed – no obstacle	21.5	1060	997.88	1975 × 1214	383	0.10	0.310
NR4	Rough bed – no obstacle	22.0	1080	997.77	1975 × 1213	327	0.10	0.309
OS1	Smooth bed – obstacle	19.0	1020	998.41	1968 × 1211	1021	0.10	0.308
OS2	Smooth bed – obstacle	20.0	1040[a]	998.20	1969 × 1210	593	0.10	0.308
OS3	Smooth bed – obstacle	19.0	1060	998.41	1972 × 1207	520	0.10	0.308
OS4	Smooth bed – obstacle	18.0	1080	998.60	1980 × 1212	441	0.10	0.308
OR1	Rough bed – obstacle	21.0	1020	997.99	1973 × 1209	981	0.10	0.308
OR2	Rough bed – obstacle	23.0	1040	997.54	1974 × 1213	609	0.10	0.308
OR3	Rough bed – obstacle	21.5	1060	997.88	1976 × 1212	489	0.10	0.308
OR4	Rough bed – obstacle	21.5	1080	997.88	1980 × 1214	450	0.10	0.307

[a]Due to a measurement error, initial theoretical density was 1040.89 kg m^{-3}; however, for simplification it is referred to as 1040 kg m^{-3}

level determined whether the current was in view of the pixel. Pixels with an intensity level lower than the threshold level were considered to be part of the background, thus replaced with a binary value of 0. Correspondingly, pixels above the threshold were considered to be within the current, thus replaced with a value of 1. The binary boundaries within each frame were traced to give vector outlines of the current. The recognized boundary was compared against raw images to assess the accuracy of the threshold level, and adjustments were made accordingly. Due to bubbles, which occasionally emitted from the siphon tubes, small regions of light pixels were incorrectly identified as being part of the turbidity current. Therefore, an algorithm was developed, which only recognized the longest vector path within an image as being the current boundary. For each image, boundaries of pixel regions above the threshold level were traced as a vector. The longest vector was considered the outline of the current, whilst shorter vectors were disregarded as light-induced noise or bubbles. Figure 3a and 3b show a comparison of the delineation with and without the longest vector algorithm applied. It can be seen that the algorithm and background subtraction provide considerable improvement in correct boundary recognition.

For each test, the range of images, N, used for velocity analysis extended from the first image where the current boundary was correctly delineated, to the last image where the current nose was visible within the analysis area (Table 1). The leading tip of the turbidity current in each image was considered to be the point on the identified boundary with the highest x/x_0 value. The spatial coordinates of this point were recorded, and the difference in horizontal distance between the current image, n, and the previous image, $n-1$, was multiplied by f to calculate the front velocity, U_n, of the current as shown in Eq. (1):

$$U_n = f\,(x_n - x_{n-1}) \tag{1}$$

This allowed time-wise velocity profiles of each test to be generated. Current interaction with the instrument arrays, and small fluctuations in light intensity due to the AC frequency of the halogen lamps, resulted in the current boundary being incorrectly delineated in some areas. This created large spikes in the front velocity analysis. Although physical darkening and background subtraction were used to minimize such noise, complete elimination was not possible. Therefore, a series of filtering techniques were applied to the data series.

A standard deviation filter based on previous work by Keevil, Peakall, Best, and Amos (2006) was applied. Time-series padding was applied to each end of the data series with a matrix of length $M = 50$, which was populated with the mean of the first and last five velocity values, respectively. The standard deviation, σ_n, of each U_n value was calculated from a 101-point moving mean as in Eq. (2) below:

$$\sigma_n = \sqrt{\frac{1}{2M+1}\left[\sum_{i=1}^{M}\left[(U_{n-i}-\mu)^2 + (U_{n+i}-\mu)^2\right] + (U_n-\mu)^2\right]} \tag{2}$$

where

$$\mu = \frac{1}{2M+1}\left[\sum_{i=1}^{M} U_{n-i} + U_{n+i} + U_n\right] \tag{3}$$

If U_n was outside $\sigma_n = 1$, it was replaced with the mean of the 50 preceding and proceeding velocities. The filter widths were chosen through a trial and error process, maximizing noise reduction whilst minimizing removal of valid data. It was also desirable to have fixed filter widths for all tests to ensure consistency and reduce processing time. However, it was found that some of the noise spikes were not adequately filtered due to their temporal duration. Therefore, these data were identified and replaced with interpolated values prior to applying the standard deviation filter (Fig. 4). Finally, all U_n values were replaced with a 20-point moving mean to calculate sub-pixel velocity values. Each end of the dataset was therefore concatenated with a 20-point matrix, which held the mean of the first and final 100 velocity values, respectively, to allow the moving mean to progress the entire width of the time series. These filter widths were chosen through a trial and error process similar to that of the standard deviation filter described above.

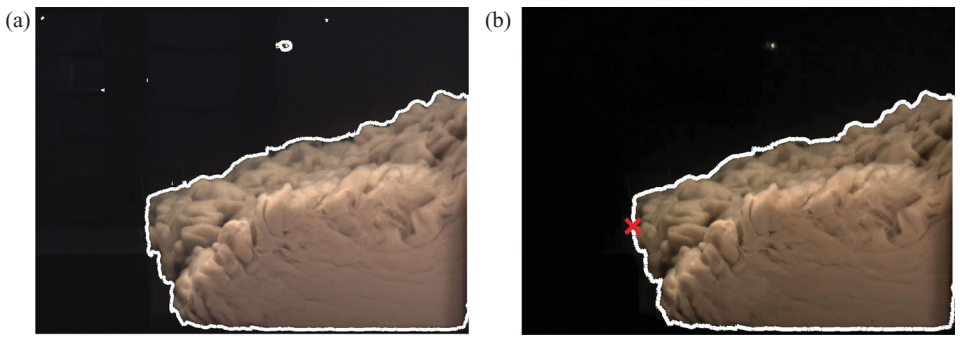

Figure 3 (a) Raw boundary delineation from thresholding technique. (b) Corrected boundary delineation by applying "longest vector" algorithm and background subtraction. Incorrect boundary recognition, including bubbles emitted from the siphons is effectively omitted. The " × " symbol represents the identified nose of the current, which is used for calculating front velocity

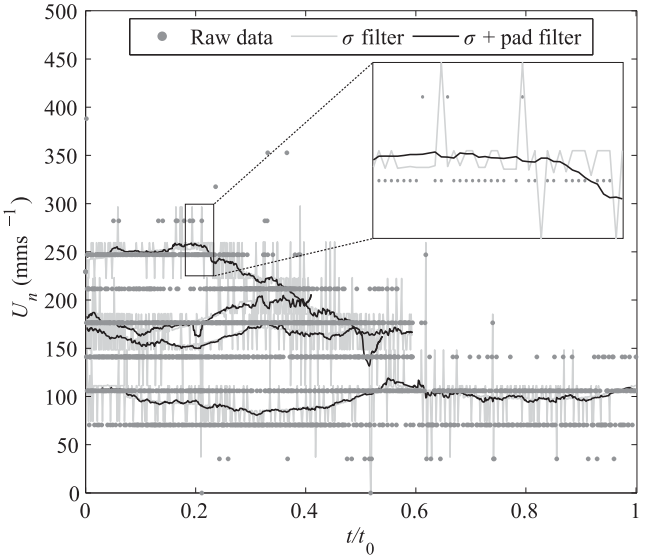

Figure 4 Velocity time series showing an example of the filtering process to remove noise spikes and obtain sub pixel velocity values. Raw data are shown as grey points; data filtered with the standard deviation filter is shown with a continuous grey linetype. The final padded data are shown with the continuous black linetype

4 Results and discussion

Figure 5a and 5b show front velocities of the currents over a smooth and rough bed, respectively. Meanwhile, Fig. 5c and 5d show front velocities for the obstacle configuration over a smooth and rough bed, respectively. For all obstacle tests where $\rho > 1020$ kg m^{-3}, there is an abrupt decay in velocity near the end of the series. This is due to the 20-point moving mean filter, which tended to underestimate the terminus velocities (shown in bold) because of the concatenated matrix. This was not present in Fig. 5a and 5b due to the comparatively consistent time series.

Figure 5a and 5b appear to show a relatively consistent velocity, within a total approximate range of 80–260 and 70–240 mm s^{-1}, respectively, showing that the rough substrate has little effect on net velocity. All series in Fig. 5c and 5d show a sharp decrease in front velocity upon impact with the obstacle, followed by a rapid increase. When the current front meets the obstacle, it is thrust upwards, causing a decrease in forward movement. The proceeding rapid increase is caused by continuation of forward movement over the obstacle. This is followed by a more gradual decrease as the current continues to distend upwards. Finally, there is a gradual increase in velocity as the current head reforms after the obstacle. When comparing initial and final velocities, the obstacle appears to reduce net velocities only slightly. Figure 5c shows that the rate of velocity flux increases with increasing current density.

4.1 *Applicability of the method*

The present approach complements rather than replaces intrusive techniques when applied to turbidity currents. The ability of UVP transducers to gain velocity profiles within the current allows insights into head and body structures and how they are transformed with the presence of an obstacle. Similarly, obtaining density contours through existing photometric techniques (Nogueira, Adduce, Alves, & Franca, 2013b) is not possible due to the opaque nature of high-density turbidity currents. At present, siphoning is still the most accepted procedure for obtaining current density profiles. Therefore, adopting a combination of measurement techniques allows a broad quantitative insight into the flow characteristics of turbidity currents (Alexander et al., 2008; Jacobson & Testik, 2013; Sequeiros et al., 2009). The illumination, binary thresholding technique and filtering processes adopted are shown to provide useful quantitative insights into flow characteristics of sediment-laden currents colliding with obstacles. Although Sequeiros et al. (2009) successfully combined a background image subtraction technique with density siphoning, they sought to highlight both the current and location of siphons within the flume. Limited guidance on their methodology is provided. In contrast, the presented method differs by using optimized illumination which minimizes the visibility of the instrument racks when background image subtraction is used. This results in clear delineation of current boundaries and also provides critical improvement over back-lit set-ups, where *in situ* instrument racks or obstacles would cause permanent visual obstruction of current boundaries (Dai, 2014; Lombardi et al., 2015; Mirajkar et al., 2015; Testik & Yilmaz, 2015; Yilmaz, Testik, & Chowdhury, 2014).

The illumination, boundary recognition and filtering techniques show a practical and effective method for obtaining photometric data from visually obstructed areas of interest. However, there are certain limitations to the technique. Firstly, the boundary recognition was shown to be effective for the tested density range of 1020–1080 kg m^{-3}, although careful consideration of illumination and threshold will be needed for lower densities, where current boundaries may not be as abrupt. Secondly, the use of the 0.307–0.310 mm/pixel ratio and high framerate resulted in a raw velocity resolution of approximately 35 mm s^{-1} (Fig. 4). Therefore, the introduction of the 20-point moving mean was necessary to obtain non-discrete velocities. As a check, the raw frames were resampled at a greater time step of $F = 12$ s^{-1}. The filtered velocities of both framerates were found to be comparable. Thus, the filtering techniques introduced provide a practical noise-reduction method. A high framerate and low mm/pixel ratio is ultimately desirable for smaller spatial areas of interest, such as that surrounding obstacles. This is to better capture the rapid temporal changes in velocity expected. However, it is recommended that if the raw velocity range does not exceed ΓF then the sampled framerate or spatial calibration factor should be decreased. The error in spatial calibration associated with camera perspective was considered acceptable; however, more investigation is needed into reducing this range where larger fields of view are desired. Future solutions for minimizing the effects may include use of

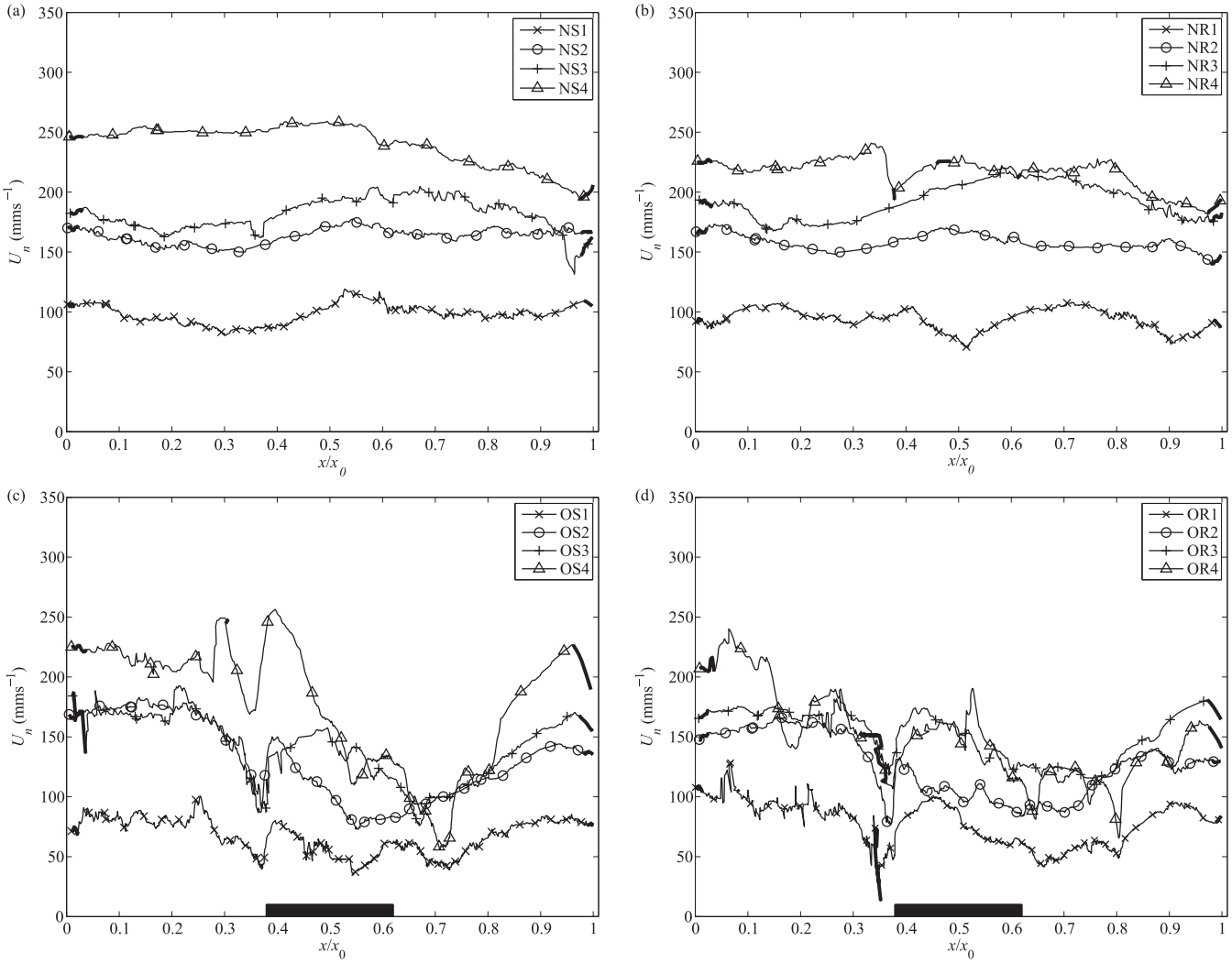

Figure 5 Horizontal front velocity as a function of non-dimensional distance for all four obstacle configurations. All velocity measurements have an error of -4.4% and $+6.0\%$. Areas of manual noise removal and approximated termini are shown with a bold linetype. The approximate horizontal extent of the obstacle is indicated in (c) and (d)

a moving camera rig relative to the current front, or use of multiple cameras with overlapping fields of view.

5 Conclusions

The aim of this study was to develop an effective thresholding methodology suitable for the study of sediment-laden currents, which allows obstacles and other visible measuring instruments to be used simultaneously with minimal impairment of image quality. Lock-exchange experiments were undertaken with varying current densities over a range of rectangular obstacle and substrate combinations. Spatial tracking and velocity data of the current front were successfully obtained with the developed binary threshold image analysis technique and optimized lighting conditions. The longest-vector algorithm, standard deviation and 20-point moving mean filtering techniques adopted are shown to significantly improve raw data quality and enable intrusive flow-measuring equipment to be successfully used in unison with photometry. This suggests substantial improvements in future studies on opaque flows, where high-frequency spatial data of current boundaries can be obtained simultaneously with other measurements, such as density and velocity profiling of turbidity current heads. However, given the increasing popularity of photometry in experimental sediment-laden and saline gravity currents, our work also highlights the need for alternative post-processing filtering techniques and subsequent comparison for a range of different testing conditions, to provide future guidelines of best practice support for photometry post-processing techniques.

Acknowledgements

The authors would like to thank the laboratory technicians Trevor Patrick, Geoff Kirby and Jim Luo for their help in constructing and installing required experimental components.

Notation

D_{50} = median sediment grain size (mm)
F = image acquisition frequency (s^{-1})
g = acceleration due to gravity (m s^{-2})
h_0 = depth of water at lock-box gate (300 mm)
I = light intensity threshold (–)
M = length of time-series padding matrix (–)
N = total number of images processed in each experimental run (–)
T = temperature of ambient fluid (°C)
t = temporal evolution of the current upon entering analysis area (s)
t_0 = time for the respective $\rho = 1020$ kg m^{-3} test to traverse the analysis area (s)
U_n = ront velocity (mm s^{-1})
x = horizontal distance of current front from upstream limit of analysis area (mm)
x_0 = horizontal length of analysis area (mm)
y = vertical height of current from flume bed (mm)
y_0 = vertical height of analysis area (mm)
Γ = pixel calibration factor (mm/pixel)
μ = mean front velocity (mm s^{-1})
ρ = initial theoretical density of turbidity current (kg m^{-3})
ρ_W = density of ambient water at measured temperature (kg m^{-3})
σ_n = standard deviation of filter window (–)

ORCID

Richard I. Wilson http://orcid.org/0000-0001-6613-3760
Craig Stevens http://orcid.org/0000-0002-4730-6985

References

Alexander, J., McLelland, S. J., Gray, T. E., Vincent, C. E., Leeder, M. R., & Ellett, S. (2008). Laboratory sustained turbidity currents form elongate ridges at channel mouths. *Sedimentology*, *55*(4), 845–868. doi:10.1111/j.1365-3091.2007.00923.x

Carter, L., Milliman, J. D., Talling, P. J., Gavey, R., & Wynn, R. B. (2012). Near-synchronous and delayed initiation of long run-out submarine sediment flows from a record-breaking river flood, offshore Taiwan. *Geophysical Research Letters*, *39*(12), L12603. doi:10.1029/2012GL051172

Cattaneo, A., Babonneau, N., Ratzov, G., Dan-Unterseh, G., Yelles, K., Bracène, R., ... Déverchère, J. (2012). Searching for the seafloor signature of the 21 May 2003 Boumerdès earthquake offshore central Algeria. *Natural Hazards and Earth System Sciences*, *12*(7), 2159–2172. doi:10.5194/nhess-12-2159-2012

Chowdhury, M. R., & Testik, F. Y. (2015). Axisymmetric underflows from impinging buoyant jets of dense cohesive particle-laden fluids. *Journal of Hydraulic Engineering*, *141*(3), 04014079. doi:10.1061/(ASCE)HY.1943-7900.0000969

Dai, A. (2013). Experiments on gravity currents propagating on different bottom slopes. *Journal of Fluid Mechanics*, *731*, 117–141. doi:10.1017/jfm.2013.372

Dai, A. (2014). Non-Boussinesq gravity currents propagating on different bottom slopes. *Journal of Fluid Mechanics*, *741*, 658–680. doi:10.1017/jfm.2014.5

Ghilardi, T., Franca, M. J., & Schleiss, A. J. (2014). Bulk velocity measurements by video analysis of dye tracer in a macro-rough channel. *Measurement Science and Technology*, *25*(3), 035003. doi:10.1088/0957-0233/25/3/035003

Heezen, B. C., & Ewing, M. (1952). Turbidity currents and submarine slumps, and the 1929 Grand Banks [Newfoundland] earthquake. *American Journal of Science*, *250*(12), 849–873.

Hsu, S.-K., Kuo, J., Lo, C.-L., Tsai, C.-H., Doo, W.-B., Ku, C.-Y., & Sibuet, J.-C. (2008). Turbidity currents, submarine landslides and the 2006 Pingtung earthquake off SW Taiwan. *Terrestrial, Atmospheric and Oceanic Sciences*, *19*(6), 767–772. doi:10.3319/TAO.2008.19.6.767(PT)

Jacobson, M. R., & Testik, F. Y. (2013). On the concentration structure of high-concentration constant-volume fluid mud gravity currents. *Physics of Fluids*, *25*(1), 016602. doi:10.1063/1.4774045

Jacobson, M. R., & Testik, F. Y. (2014). Turbulent entrainment into fluid mud gravity currents. *Environmental Fluid Mechanics*, *14*(2), 541–563. doi:10.1007/s10652-014-9344-5

Keevil, G. M., Peakall, J., Best, J. L., & Amos, K. J. (2006). Flow structure in sinuous submarine channels: Velocity and turbulence structure of an experimental submarine channel. *Marine Geology*, *229*(3-4), 241–257. doi:10.1016/j.margeo.2006.03.010

Lombardi, V., Adduce, C., Sciortino, G., & La Rocca, M. (2015). Gravity currents flowing upslope: laboratory experiments and shallow-water simulations. *Physics of Fluids*, *27*(1), 016602. doi:10.1063/1.4905305

Longo, S., Ungarish, M., Di Federico, V., Chiapponi, L., & Maranzoni, A. (2015). The propagation of gravity currents in a circular cross-section channel: experiments and theory. *Journal of Fluid Mechanics*, *764*, 513–537. doi:10.1017/jfm.2014.701

Marino, B. M., Thomas, L. P., & Linden, P. F. (2005). The front condition for gravity currents. *Journal of Fluid Mechanics*, *536*, 49–78. doi:10.1017/S0022112005004933

Marleau, L. J., Flynn, M. R., & Sutherland, B. R. (2015). Gravity currents propagating up a slope in a two-layer fluid. *Physics of Fluids*, *27*(3), 036601. doi:10.1063/1.4914471

Mirajkar, H. N., Tirodkar, S., & Balasubramanian, S. (2015). Experimental study on growth and spread of

dispersed particle-laden plume in a linearly stratified environment. *Environmental Fluid Mechanics*, 1241–1262. doi:10.1007/s10652-015-9412-5

Nogueira, H. I. S., Adduce, C., Alves, E., & Franca, M. J. (2013a). Analysis of lock-exchange gravity currents over smooth and rough beds. *Journal of Hydraulic Research*, *51*(4), 417–431. doi:10.1080/00221686.2013.798363

Nogueira, H. I. S., Adduce, C., Alves, E., & Franca, M. J. (2013b). Image analysis technique applied to lock-exchange gravity currents. *Measurement Science and Technology*, *24*(4), 047001. doi:10.1088/0957-0233/24/4/047001

Nogueira, H. I. S., Adduce, C., Alves, E., & Franca, M. J. (2014). Dynamics of the head of gravity currents. *Environmental Fluid Mechanics*, *14*(2), 519–540. doi:10.1007/s10652-013-9315-2

Sequeiros, O. E., Naruse, H., Endo, N., Garcia, M. H., & Parker, G. (2009). Experimental study on self-accelerating turbidity currents. *Journal of Geophysical Research-Oceans*, *114*(C5), 1464. doi:10.1029/2008JC005149

Stagnaro, M., & Bolla Pittaluga, M. (2014). Velocity and concentration profiles of saline and turbidity currents flowing in a straight channel under quasi-uniform conditions. *Earth Surface Dynamics*, *2*(1), 167–180. doi:10.5194/esurf-2-167-2014

Testik, F. Y., & Yilmaz, N. A. (2015). Anatomy and propagation dynamics of continuous-flux release bottom gravity currents through emergent aquatic vegetation. *Physics of Fluids*, *27*(5), 056603. doi:10.1063/1.4919783

Wilson, R. I. (2015). *Optimisation of lighting techniques for photometric measurement of sediment-laden flows*. Paper presented at the 36th International IAHR World Congress, The Hague, the Netherlands. IAHR. Retrieved from https://www.iahr.org/site/cms/contentdocumentview.asp?chapter=42&documentid=2554&category=344&article=1014.

Yilmaz, N. A., Testik, F. Y., & Chowdhury, M. R. (2014). Laminar bottom gravity currents: Friction factor–Reynolds number relationship. *Journal of Hydraulic Research*, *52*(4), 545–558. doi:10.1080/00221686.2013.878402